

# Ultra-Wideband Joint Spatial Coding for Secure Communication and High-Resolution Imaging

Himanshu Aggrawal, *Student Member, IEEE*, Rafael Puhl,  
Christoph Studer, *Senior Member, IEEE*, and Aydin Babakhani, *Member, IEEE*

**Abstract**—This paper introduces new techniques for ultra-wideband joint spatial coding in order to establish a secure line-of-sight (LOS) wireless communication link, performing precision localization of point objects, and generating high-resolution images from complex scenes. For the proposed technique, symbol generation and coding are jointly performed by multiple widely spaced transmitters. This method enables the transmission of directionally-modulated signals that can only be decoded at a desired angle, resulting in a secure communication link. It is also shown that joint spatial coding by multiple transmitters that are synchronized with each other enables the precise localization of multiple point objects and allows high-resolution three-dimensional imaging of distributed objects. The technique is demonstrated experimentally in the frequency range 3–10 GHz by generating and detecting ultra-wideband pulses.

**Index Terms**—Analog, coherent, encryption, imaging, localization, pulse, radar, secure communication, synchronized, time-of-flight, ultra-wideband

## I. INTRODUCTION

The generation, radiation, and detection of electromagnetic waves have come a long way since the invention of the transistor in the early 1950s. Since then, we have developed integrated circuits that form the backbone of the modern digital revolution. Today’s silicon technology provides transistors with  $f_T$  and  $f_{max}$  of higher than 300 GHz. This paradigm shift has opened the door to many exciting opportunities for the millimeter-wave and THz research. These advances in silicon technology have enabled the generation and detection of picosecond pulses, which opens a variety of new possibilities. Due to the small wavelengths of millimeter and THz waves, the applications include (but not limited to) high-speed secure wireless communication, three-dimensional (3D) radar imaging, spectroscopy, wireless time-transfer, and many more [1]–[5].

In this work, we propose an ultra-wideband joint spatial coding technique which enables substantial improvements in the security of LOS wireless communication links and in the resolution of 3D radar imaging systems. Such communication systems are particularly useful where point-to-point communication security is of paramount importance—for example, communication in a military environment. High-resolution imaging can, for example, be used for airport security (replacing conventional mm-wave scanners), medical imaging, and gesture recognition. In this paper, joint spatial coding is

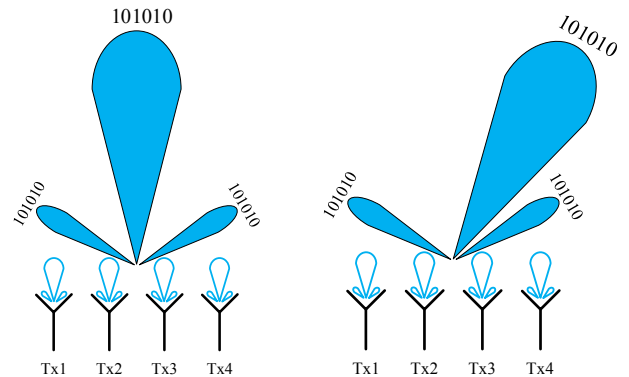


Fig. 1. Conventional beamforming of continuous wave (CW) based systems. The complete transmit information is present in the main lobe as well as in the side lobes. Any eavesdropper can receive and decode the information present in the side lobes.

demonstrated using ultrashort pulses occupying the frequency band of 3–10 GHz, as a proof-of-concept. The performance of the proposed techniques can be improved further by using even shorter pulse-widths.

The remainder of the paper is organized as follows. Section II discusses how the proposed technique can be used to establish a secure LOS communication link. Section III focuses on the applications of this technique in localizing point objects. Section IV discusses the use of this technique in imaging complex scenes. Section V concludes the paper.

## II. SECURE WIRELESS COMMUNICATION LINKS

In conventional line-of-sight (LOS) wireless communication links, information generation is done at a single location in space. In these architectures, although the radiated power is focused at a desired angle that is determined by the antenna radiation pattern [6], the information content is released to all directions in space. In other words, an eavesdropper that is equipped with a sensitive receiver [7] located outside of the main antenna lobe observes the same, but attenuated, time-domain waveform transmitted to the desired angle, as illustrated in Fig. 1. Recently, the concept of Near-Field Direct Antenna Modulation (NFDAM) [8] or directional modulation [9] was introduced to increase the security of communication links by generating information jointly with multiple transmitters, resulting in a directional modulation scheme. In these architectures, the time-domain waveform transmitted to a desired direction differs from the waveform transmitted to other angles, preventing eavesdroppers from cap-

H. Aggrawal, R. Puhl, and A. Babakhani are with the Department of Electrical and Computer Engineering, Rice University, Houston TX; e-mail: himanshu@rice.edu, rafaelbidese@gmail.com, aydin.babakhani@rice.edu

C. Studer is with the School of Electrical and Computer Engineering, Cornell University, Ithaca, NY; e-mail: studer@cornell.edu

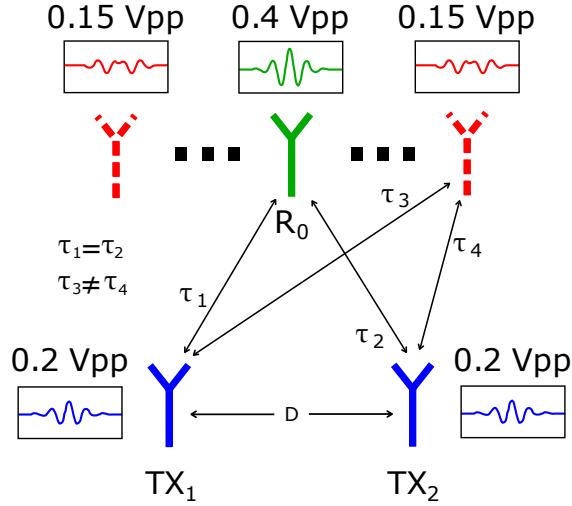


Fig. 2. Information generation with two tightly synchronized impulse transmitters. The correct information is only present at the desired location.

turing the transmitted information signal. Traditional directional modulation transmitters [9], [10] operate with narrow-band signals, which limits their performance.

#### A. Joint Spatial Coding

For secure wireless communication, the key technique is to separately encode signals on different transmitting antennas such that the information itself is a function of spatial location. Hence, the received information is different at each physical location and only the targeted location containing the target recipient can correctly decode the transmission. This feature fundamentally transforms the weakly secure concept of energy focused into a beam into a new paradigm of information focused in space. We have shown that the spatial resolution for correct decoding can be confined to a custom 3D area at wavelength scale (millimeters). We propose a spatial encoding architecture in which we tightly synchronize [5] multiple widely spaced transmitting antennas at the symbol level to generate information that is focused to a small spatial location and cannot be decoded from a reflected path, nor from in front of or behind the intended target location. Our technique shapes pulses across antennas with different portions of the information encoded on different antennas. This contrasts with conventional wireless communication systems in which the complete constellation symbol is transmitted from one antenna, or in the case of highly directional phased arrays, from all antennas via a phase offset per antenna. Spatial encoding fundamentally differs in its topology: instead of sending the complete constellation symbol (complete information) from a single antenna, a part of the symbol (semi-symbol), which is a fraction of the total amplitude, is sent from one antenna and the remaining fraction is sent from other antennas. The transmitting antennas are synchronized at the symbol level. A receiver that is placed exactly at the focus point, where all the semi-symbols arrive at the same time, adding coherently to the complete symbol. The point where all the semi-symbols combine coherently is

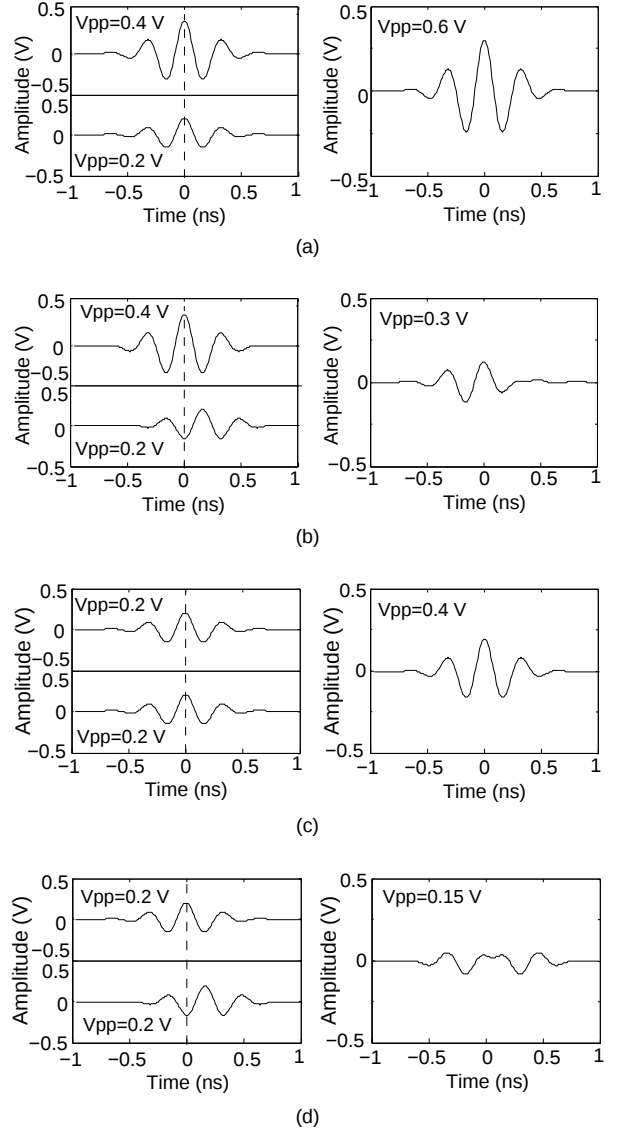


Fig. 3. The effect of time-delay in corrupting the time-domain waveforms. (Left) Time-domain signals generated by each antenna. (Right) The combined signal. (adapted from [2]).

unique in space, and thus, the communication can be said to be spatially encoded.

The spatial encryption is illustrated with two transmitting antennas, as shown in Fig. 2.  $s_{\text{orig}}(t)$  denotes the complete time-domain symbol. This signal is divided into two semi-symbols,  $s_1(t)$  and  $s_2(t)$ , such that  $s_{\text{orig}}(t) = s_1(t) + s_2(t)$ . The signal  $s_1(t)$  is generated by transmitter 1 (TX<sub>1</sub>) and  $s_2(t)$  is generated by transmitter 2 (TX<sub>2</sub>) using a two-channel arbitrary waveform generator. Let  $\tau_1$  and  $\tau_2$  be the propagation delays from TX<sub>1</sub> and TX<sub>2</sub> to a point  $P$  in space, respectively. The received signal in space is given by  $s_1(t - \tau_1) + s_2(t - \tau_2)$ . When the point  $P$  is spaced equidistantly from TX<sub>1</sub> and TX<sub>2</sub>, both signals arrive at the same time, add coherently, and the desired symbol  $s_{\text{orig}}(t)$  is generated. In contrast, if the point  $P$  is not spaced equidistantly from the two transmitters,  $s_1(t)$  and  $s_2(t)$  arrive at different times, which results in a corrupted time-domain waveform. Although this idea is described for

TABLE I  
SYMBOL GENERATION AT A DESIRED ANGLE WITH TWO TRANSMITTING ANTENNAS. (ADAPTED FROM [2])

Tx1 {Semi-symbol} (V)	0.1	0.1	0.2	0.1	0.2	0.3	0.1	0.2	0.3	0.4	0.2	0.3	0.4
Tx2 {Semi-symbol} (V)	0.1	0.2	0.1	0.3	0.2	0.1	0.4	0.3	0.2	0.1	0.4	0.3	0.2
Tx1+Tx2 {Complete symbol} (V) [Bits]	0.2	0.3	[00]	0.4	[01]			0.5	[10]			0.6	[11]

two transmitters ( $T_{x1}$  and  $T_{x2}$ ) and one receiver ( $R_x$ ), it can be scaled to multiple transmitters and receivers.

Now let us assume that the two synchronized transmitters have amplitude modulation capability, each with an accuracy of two bits. For a receiver equidistant from the transmitters, the received signal will be the sum of the transmitted signals (semi-symbols). Assume the bits “00”, “01”, “10”, and “11” correspond to peak-to-peak voltages of 0.3 V, 0.4 V, 0.5 V, and 0.6 V, respectively, as shown in Table I. As shown in this table, some of the complete symbols (for example, 0.4 V) can be generated by different weightings between two transmitters. These different weightings will result in the same complete symbol, as long as the received is equidistant from the transmitters. For non-equidistant receivers, the semi-symbols will experience different delays, which will result in partial overlapping or no overlapping of the semi-symbols in the time-domain. Thus, the received symbol will be distorted, as shown in Fig. 3. If the receiver uses a lookup table (Table I), this incorrect amplitude will correspond to a different bit and it will be decoded erroneously.

All the possible combinations of transmitted and received symbols for an equidistant receiver antenna are tabulated in Table I.

1) *Semi-symbol selection*: The final symbol to be sent determines the pair of semi-symbols to be generated and the transmitters pseudo-randomly choose one of the possible semi-symbol pairs, as shown in Table I.

2) *Matching received signal to a look-up table*: A look-up table is created to match the received amplitudes to the corresponding bits. This look-up table is generated for

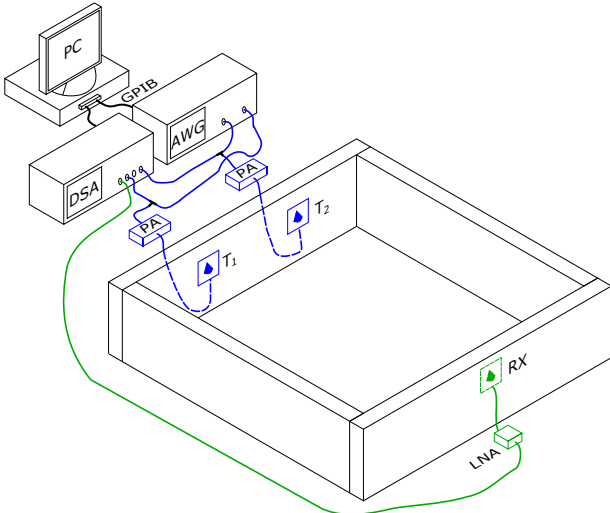


Fig. 4. Experimental setup to demonstrate spatial encryption.

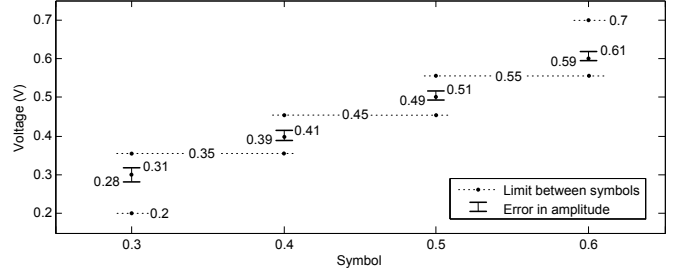


Fig. 5. Setting threshold midway between the symbol voltages (adapted from [2]).

equidistant receiver during the training period.

3) *Beam steering and focusing*: The location of the desired receiver can be moved by introducing proper delays in the transmitters. The point in space where all the semi-symbols coherently combine is controlled by the relative delays introduced in the transmitters. A receiver located at this point will achieve the lowest bit error rate. The convenience of changing the location of the desired receiver by introducing relative delays in the transmitters is one of the highlights of this architecture.

## B. Experimental Results

In order to experimentally demonstrate the concept, a two channel arbitrary waveform generator (Tektronix AWG7122C) with internally locked channels is used. This arbitrary waveform generator produces ultra-short pulses, which are then amplified (RF-Lambda RLNA02G18GA) and radiated using a custom impulse antenna. A similar antenna is used at the input of the receiver. The received signal is then amplified by an LNA (Mini-Circuits ZX60-14012I-S+) before being sampled by a real-time oscilloscope (Tektronix DSA71804B). Fig. 4 shows the experimental setup. The photograph of the setup is shown in Fig. 8.

The measurement system is calibrated before the bit error rate (BER) test is performed. During the calibration period, the non-

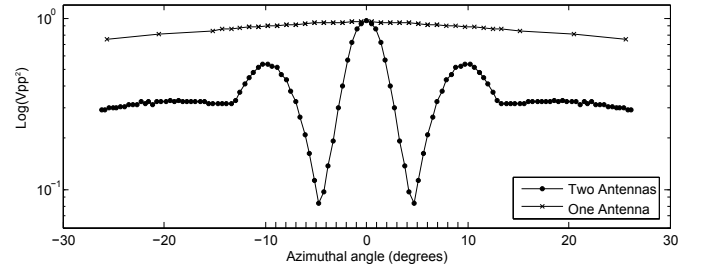


Fig. 6. Effective radiation patterns of a single antenna and two coherently transmitting antennas (adapted from [2]).

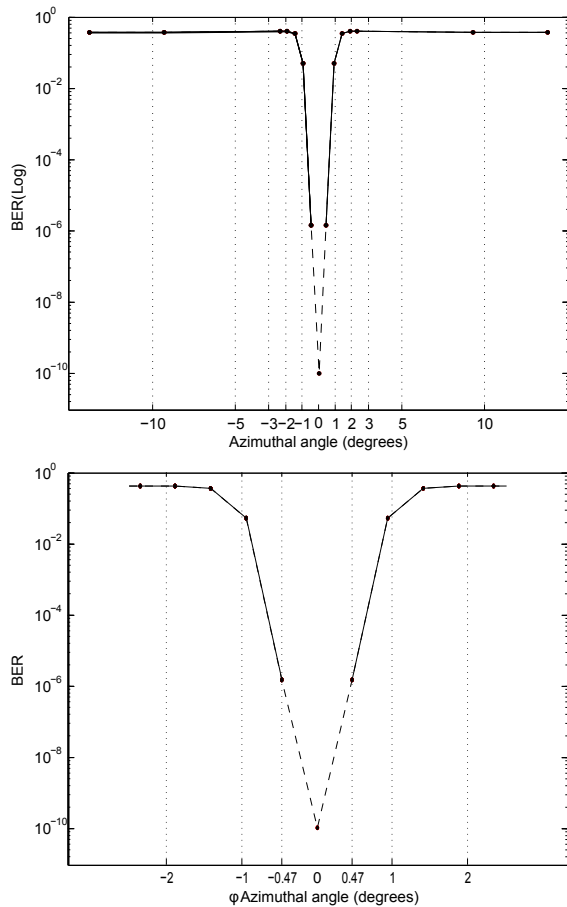


Fig. 7. Measured bit error rate (BER) of the system. (Top) Measurement across a wide range of azimuthal angle, (Bottom) Zoomed version between  $0-2^\circ$ . The BER measurement was done for the left side and mirrored the right side, leveraging symmetry in the system (adapted from [2]).

linearity of the amplifier is compensated by pre-distorting the semi-symbols. To pre-distort the semi-symbols, first, a voltage ramp is generated and transmitted after being amplified by the power amplifier. The transmitted ramp is received and amplified by LNA before being captured by an oscilloscope (Fig. 4). The received ramp is distorted because of the non-linearities of the amplifier in the signal chain. Next, the transmitted ramp is pre-distorted such that the received ramp is linear. The final semi-symbol points are chosen on this pre-distorted ramp to receive the correct amplitude at the receiver. Even after the pre-distortion there are slight variations in the received voltages. This is due to non-linearities in the system and to channel effects. For example, if bit “01” is transmitted with all possible semi-symbol combinations, the receiver should receive an amplitude of 0.4 V. Due to the non-idealities in the measurement, the received signal amplitude ranges from 0.39 V to 0.41 V (Fig. 5). To assign received voltages to digital bits, threshold levels are set between the symbol voltages, as shown in Fig. 5. For instance, the ideal received voltage for bit “01” is 0.4 V and for bit “10” is 0.5 V. A threshold is set at 0.45 V. If the received signal amplitude is less than 0.45 V, bit “01” is detected else bit “10” is detected.

The radiation pattern of a single impulse antenna can be

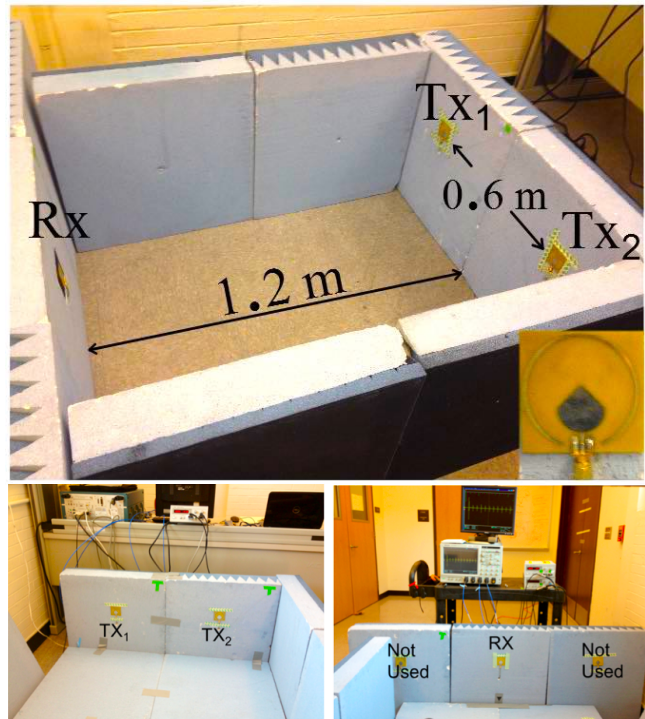


Fig. 8. Experimental setup to demonstrate spatial encryption (partially adapted from [2]).

plotted by measuring the power of the radiated pulse as a function of angle. The radiation pattern of one such used antenna is very broad, as shown in Fig. 6. However, for the case of two synchronized transmitting antennas, the combined radiation pattern, generated by the sum of two coherent signals transmitted by two antennas, becomes very narrow. This is because as we move away from the center of the antennas, the signals no longer combine coherently and the power drops exponentially.

The robustness of a communication link is determined by

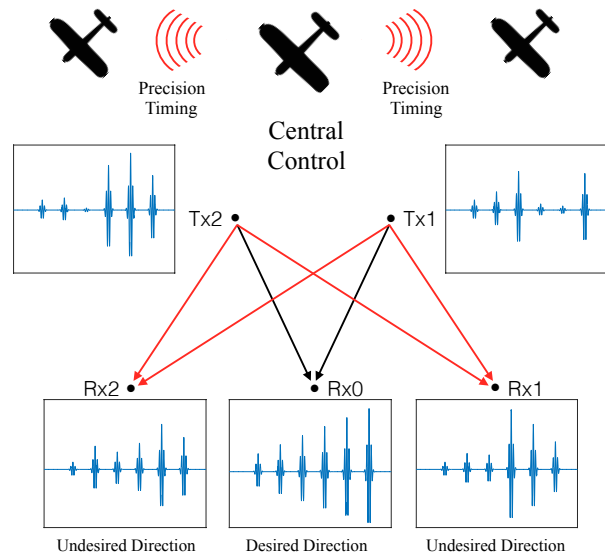


Fig. 9. Application of spatially secure point-to-point communication

measuring the BER of the system. The BER of this link is measured by using a pseudo-random number generator to generate the transmit data. The symbols to be transmitted are determined by the data to be transmitted. These symbols are broken down into pairs of semi-symbols, chosen randomly from Table I. The look-up table is used to convert the received amplitude to corresponding bits. Finally, comparing the transmitted and received bits gives us the BER.

The spatial information distribution of a communication link is represented by plotting the BER as a function of spatial distribution [2]. As shown in Fig. 7, a BER of  $10^{-2}$  at  $1^\circ$  and  $10^{-6}$  at  $0.47^\circ$  were measured. A linear extrapolation of these results gives a BER of less than  $10^{-10}$  at the center. The sharpness of the BER curve shows how narrow the spatial information distribution of this communication link is (information beamwidth), even though the individual radiation pattern of the single impulse antenna is relatively broad.

### III. LOCALIZATION OF POINT OBJECTS

The ability to localize and image objects has significant importance in radar and collision avoidance systems [11]–[13]. Techniques like time-of-flight (ToF) and angle-of-arrival (AoA) have been used to triangulate the location of objects [14]–[16]. Most CW radars are based on frequency modulated (i.e., FM-CW radars) [17], [18]. These radars have very narrow bandwidth and limited range, and they suffer from ambiguity due to the Doppler effect. Recently, ultra-wideband localization systems have been introduced [14], [19], [20]. These systems are more accurate than traditional FM-CW systems. However, the inherent limitation of ToF/AoA architecture makes it impossible for them to be used to image complex scenes. This section explores the limitations of ToF/AoA and then introduces a novel linearization-based imaging approach for complex imaging.

In this section, point objects are localized using ultra-short pulses and time-of-flight measurements (i.e., the time taken by the pulse to travel to the object, get reflected, and travel back to the transmitter). A locus of points whose total distance from two points (transmitter and receiver) is constant forms an ellipse, as shown in Fig. 10. As shown in this figure, the method of triangulation with multiple ellipses can be used to localize an object.

The block diagram of the experimental setup is shown in Fig. 11. A two-channel arbitrary waveform generator (Tektronix AWG7122C) is connected to the power amplifiers, each with 25 dB gain to generate the transmitted pulses. These signals are radiated with impulse antennas. A similar impulse antenna is

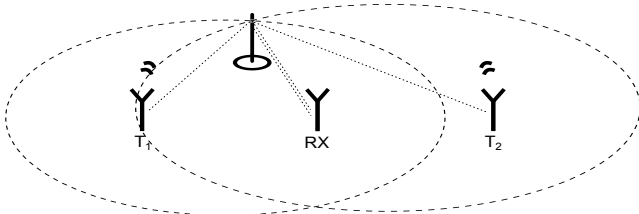


Fig. 10. Time-of-flight triangulation for localizing an object

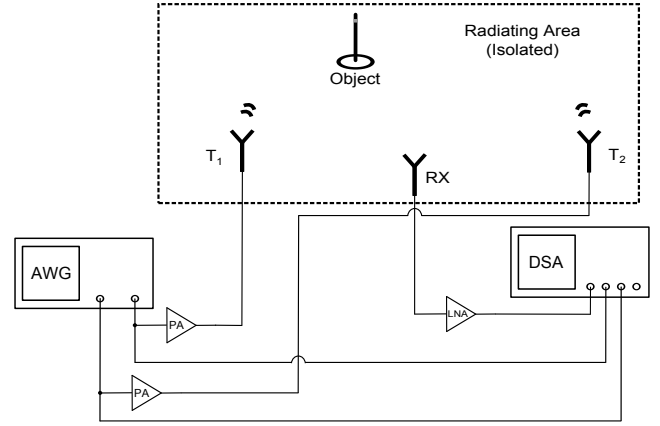


Fig. 11. Experimental setup for pulse-based time-of-flight localization

used as a receiver, the signal of which is amplified by a 30 dB gain LNA before being sampled by an oscilloscope. A copy of the original transmitted pulse signal is also recorded by an oscilloscope (Tektronix DSA71804B) to determine the time of flight. In this experiment, the distance between the transmitters is 940 mm and the receiver is placed in the middle but 150 mm behind the transmitters to reduce the direct coupling between the transmitters and the receiver.

The object to be localized is an acrylic rod with 12.5 mm in diameter. Because acrylic has a very weak radar cross section, a small stripe of aluminum foil, 10 mm in height, is wrapped around the rod such that the middle of the stripe is at the same height as the center of the antennas. All acquisitions are automated using a GPIB-VISA protocol.

The reflected pulses from the object are amplified and

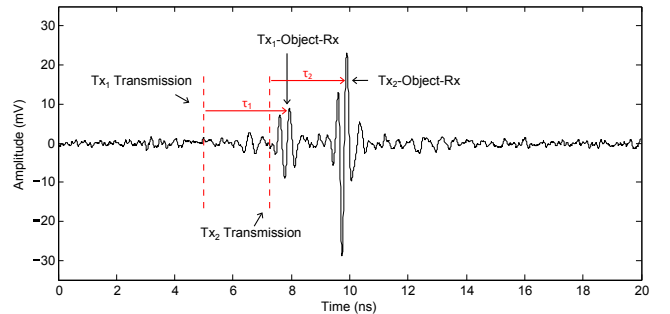


Fig. 12. Reflected signal received by the receiver

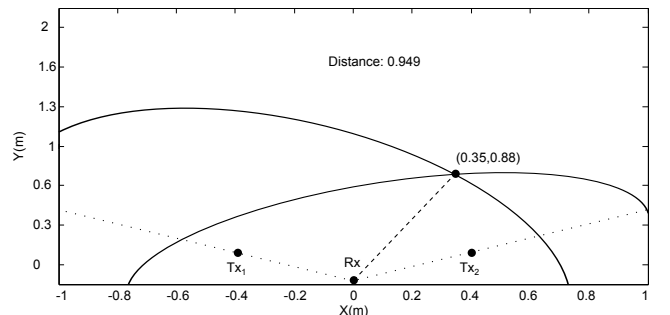


Fig. 13. Triangulation after receiving the signal

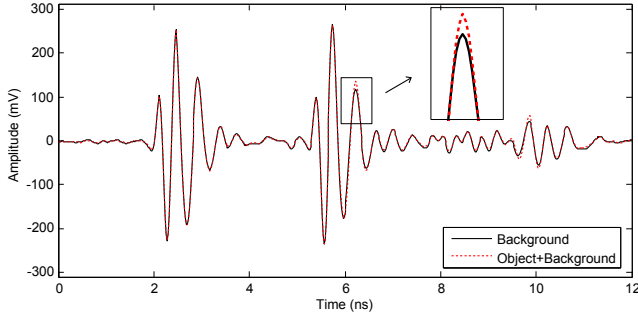


Fig. 14. Received signal in the absence and presence of the object

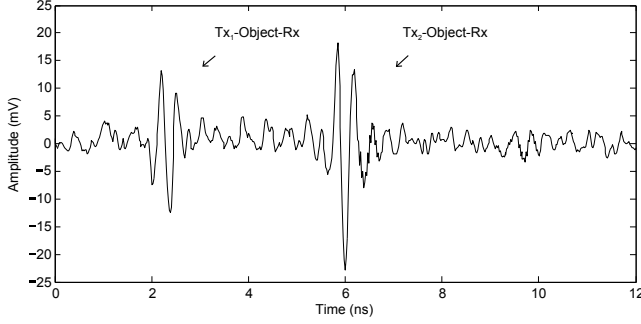


Fig. 15. Received signal after subtracting the background signature

recorded by an oscilloscope. The measured time of flight is multiplied by the speed of light to calculate the round-trip distance between the transmitter, the object, and the receiver. Knowing the distance between the transmitter and the receiver, an ellipse on which the object lies can be drawn. Several transmitter/receiver pairs can be used to generate multiple ellipses to triangulate the exact location of object(s).

Fig. 12 shows the reflected signal and the time delay caused by the longer travel path. Fig. 13 shows the intersection of the ellipses to triangulate the location of the object.

It is crucial to calibrate the setup as the experiments are both time and distance sensitive. A two-stage calibration process was deployed. During stage one, the cable lengths were adjusted in such a way that both the transmitted signals reach the antennas at the same time. Also, the delay in the signal path from transmitter to antenna and antenna to receiver was carefully measured. These data are later used in distance estimation.

In stage two, ultra-short pulses ( $\sim 200$  ps pulse width) are radiated using the impulse antennas. The object is removed from the scene (imaging arena) and the reflected signal is recorded. This captured time-domain signal contains data about the background and its reflection signature. This signature is later subtracted from the reflected signal of the scene with the object present to increase the SNR of the system. Fig. 14 shows the reflected signal with and without the object. Fig. 15 shows the change in reflection signature due to the presence of the object by subtracting the reflected signal with an object from the reflected signal without an object.

1) *Single object localization*: To validate the proposed architecture, various experiments were performed to accurately determine the location/position of the object. This was done by placing an object on a one-dimensional travel table that

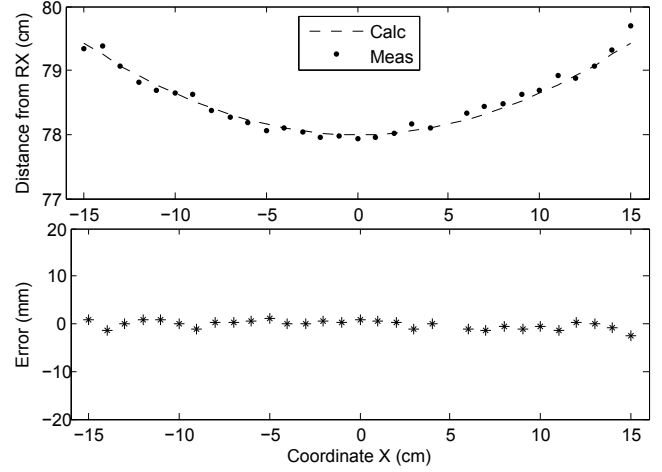


Fig. 16. Total distance transmitter-object-receiver.

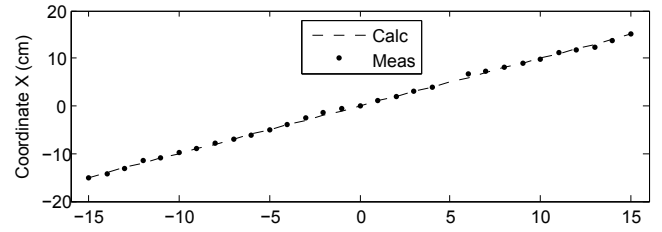


Fig. 17. X-coordinate of the object during the sweep measurement.

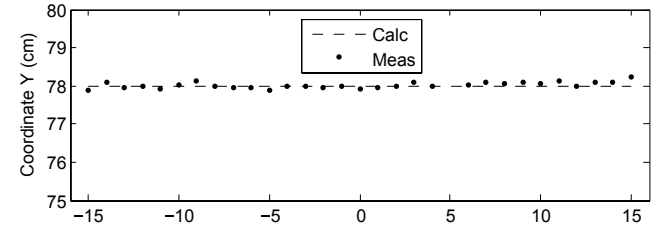


Fig. 18. Y-coordinate of the object during the sweep measurement.

can travel 300 mm with an accuracy of 0.01 mm. The rail was in alignment with the receiver antenna such that the object moved from 150 mm left of the receiver to 150 mm right of the receiver, with steps of 10 mm, at a fixed perpendicular distance of 780 mm from the receiver antenna. Such an orientation was chosen because even though the object was moving in only one-dimension, the total round trip distance changes parabolically, thus emulating two-dimensional motion. The dashed curve in Fig. 16 is the exact distance of the object from the receiver during the sweep. The dots represent the measured distance using the reported technique. It can be seen that the divergence of the measured distance over the actual distance is small and that the variance is of the order of a few millimeters. Shown in Fig. 17 and Fig. 18 are the exact and calculated X,Y co-ordinates of the object. Because the object is moving in X-direction, the X coordinates increase linearly while the Y coordinates stay the same.

2) *Multiple object localization*: Multiple object imaging can be viewed as imaging discrete points. This assumption is valid if the objects are small (i.e., single-point reflection is

valid {Object size  $\ll$  Object distance and Object size  $\ll$  Pulse length in the medium}), at a considerable distance from each other, and do not occlude the radar signal. If such a pattern is followed, multiple ellipses can be drawn to triangulate the position of each point object. However, the above assumption is not always true and then, imaging such a cluster is not trivial. Another way to tackle this problem is beam-forming and raster scan. Multiple transmitters can be used to beamform the pulses to a particular point in 3D space. In pulse-based systems, beamforming is done by adjusting the delays of the transmitted pulses to sum coherently at a single point, where the total power received is  $N^2$  ( $N$  being the number of transmitting antennas). This point is swept in  $X, Y$  and  $Z$  to get an accurate depth image. However, one major disadvantage of this system is the scan time, which makes it unsuitable for videography or for imaging moving objects. Since the existing hardware is limited to two transmitters and four real-time receivers, a novel mathematical model for imaging with multiple transmitters and receivers is introduced in the next section that is capable of imaging complex and distributed objects.

#### IV. IMAGING OF COMPLEX SCENES

In scenarios where only one small object is present in front of a pair of transmitters and receivers, the simple triangulation approach discussed in Section III is sufficient to identify their exact spatial location. For scenes that contain more complex or multiple objects, such as the one illustrated in Fig. 19, triangulation is no viable solution. Hence, in order to enable imaging using the time-of-flight approach for complex scenes, alternative methods to triangulation become necessary (see [21]–[23] and the references therein). Reference [24] proposed a frequency-modulated continuous-wave (FMCW) radar approach that can be used for real-time through-wall imaging. Reference [25] demonstrated imaging using an ultra-wideband synthetic aperture radar. The authors proposed a range-point migration technique to suppress undesirable arc-shaped artifacts. Reference [26] used UWB pulses to detect breast cancer. Their primary methodology required the knowledge of the difference in the dielectric constant between the healthy and cancerous tissue, thus limiting its scope. All of the methods in [24]–[26] show promising results for simple scene reconstruction, but do not provide strategies to perform imaging of complex scenes with occluded objects. Their main principle, however, could be combined with the approach proposed next.

We now describe a new linearization-based imaging approach that enables the efficient recovery of complex scenes from time-of-flight information. Our idea is to scale up the localization system discussed in Section III to a larger transmit/receive array, which can be used in combination with a novel recovery algorithm to image complex scenes at low complexity. We demonstrate the efficacy of the proposed approach using simulation results.

##### A. Imaging System, Scene Model, and Recovery Problem

We assume an array of antennas consisting of  $M_T$  transmitters and  $M_R$  receivers, which is placed at one side of the

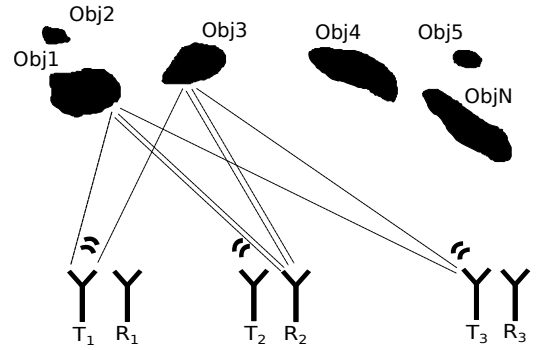


Fig. 19. Illustration of the proposed pulse-based time-of-flight imaging system consisting of  $M_T = 3$  transmitters and  $M_R = 3$  receivers. The goal is to recover scenes containing multiple complex objects.

scene to be imaged (see Fig. 19). We then emit short pulses from all transmitters and measure the signals at all receivers as detailed in Sections II and III. The ultimate goal is to recover the scene (i.e., localize and image the objects) solely using the received time-of-flight information.

Instead of using triangulation, we propose to discretize the scene (or area) to be imaged into multidimensional mesh consisting of  $N$  square cells  $x_i$ ,  $i = 1, \dots, N$ . If there is a reflecting object within the  $i$ th cell, then we assume that  $x_i = 1$ ; for an empty cell, we assume  $x_i = 0$ . Fig. 20 shows a 2-dimensional scene example that contains two contiguous and large objects; the scene has been discretized into a  $20 \times 26$  cell grid ( $N = 520$ ).

From the receive signals measured at all  $M_R$  receivers, our goal is to recover the occupancy information contained in  $x_i$  for each cell. Unfortunately, scene recovery is a nontrivial task. Consider, for example, the situation illustrated in Fig. 20. Here, an object is occluded by another reflecting (or non-transparent) object, i.e., invisible to (some of) the transmitters and receivers.

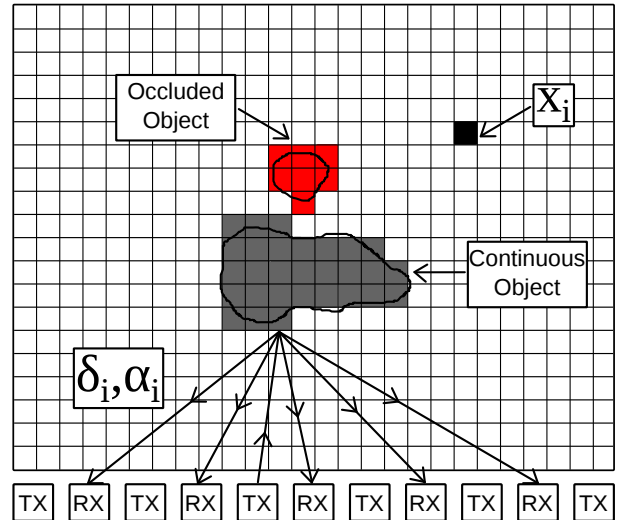


Fig. 20. Scene discretization and illustration of a scene where an object (red) is occluded by another object (grey). Scene recovery tries to identify the occupancy information contained in each cell  $x_i$  using the received signals.

By solely considering the acquired signals, recovery of the occluded object is impossible—its presence does not affect the receive signals. Generally speaking, the occupancy of a cell  $x_i$  may affect the delay and amplitude patterns of another object in cell  $x_{i'}$ , if an object in cell  $i$  is on a reflection path of an object in cell  $i'$  and vice versa. As a consequence, the receivers do, in general, not see a linear superposition of reflection information from occupied cells, which results in a challenging non-linear scene recovery problem that requires sophisticated scene recovery algorithms.

### B. Linearized Scene Model

In order to arrive at a computationally efficient way to recover such complex scenes, we propose to linearize the system. The approach discussed in the following is inspired by the method put forward in [27], which uses a linearization strategy to detect objects in a light-curtain application.

Assume that only one transmitter is active and that only the  $i$ th cell is occupied in the scene. For this situation, we can characterize the reflected signals that are measured at each of the  $j = 1, \dots, M_R$  receivers by their respective total travel time  $\delta_{j,i}$  of the transmitted pulse and their attenuation  $\alpha_{j,i}$  that occurs on the paths to be reflected. Hence, we can compute a so-called “occupancy signature,” which is characterized by received time-domain signals at all  $M_R$  receivers assuming that only the  $i$ th cell is occupied. The main assumption underlying the proposed linearized approach is that the occupancy of one cell does not affect any other cell. This assumption leads to a model for which all received time-domain signals are simply a linear superposition of the occupancy signatures from all cells that are occupied with reflective material.

More formally, we discretize the scene into an  $N$ -dimensional occupancy vector  $\mathbf{x} \in \{0, 1\}^N$  (the information of a discretized 2-dimensional scene is converted into one long vector) and model the measured signals at the  $M_R$  receivers using the following linear, noisy input-output relation:

$$\mathbf{r} = \Phi \mathbf{x} + \mathbf{n}. \quad (1)$$

Here, the vector  $\mathbf{r} \in \mathbb{R}^{TM_R}$  contains all measured information at the  $M_R$  receivers over  $T$  time-domain samples, the matrix  $\Phi \in \mathbb{R}^{TM_R \times N}$  is defined by all  $N$  occupancy signatures, and the vector  $\mathbf{n} \in \mathbb{R}^{TM_R}$  models additive noise in the system.

The remaining piece of the proposed model is the construction of the matrix  $\Phi$ , which can be performed offline for a given setup. In particular, one must fix all system parameters, i.e., the number and locations of the transmitters and receivers, the discretization of the scene to be recovered, and the pulse waveforms as well as the time instants where each pulses at every transmitter is emitted. For each of the  $N$  cells, one can then assume that only the  $i$ th cell is occupied and compute the time-domain signal at each of the  $M_R$  receivers, assuming that pulses at all  $M_T$  transmitters were emitted. We can then stack all  $M_R$  received time-domain signals into a column vector  $\phi_i$ , which simply corresponds to the  $i$ th column of the matrix  $\Phi = [\phi_1 \cdots \phi_N]$ . This matrix can be constructed off-line using a physical model of the imaging setup.

### C. Low-Complexity Scene Recovery

For a given system setup and a given scene, the matrix  $\Phi$  and the vector  $\mathbf{r}$  are given. Hence, the remaining task is to compute an estimate of the occupancy vector  $\mathbf{x}$  using this information. By assuming i.i.d. Gaussian noise for the entries of the vector  $\mathbf{n}$ , the optimum recovery problem for the linearized system in (1) is given by

$$\hat{\mathbf{x}} = \arg \min_{\mathbf{x} \in \{0,1\}^N} \|\mathbf{r} - \Phi \mathbf{x}\|_2, \quad (2)$$

where  $\|\cdot\|_2$  represents the Euclidean (or  $\ell_2$ ) norm. Unfortunately, the binary constraint in (2) causes this problem to be of combinatorial nature whose complexity is known to grow exponentially in the number of cells  $N$  [28].

In order to arrive at a scene recovery method that can be implemented in practice, we propose to relax the binary-valued constraint  $\mathbf{x} \in \{0, 1\}^N$  to  $\mathbf{x} \in \mathbb{R}^N$ , which leads to an unconstrained least-squares problem that can be solved at low complexity. In fact, this LS problem has a closed-form solution  $\tilde{\mathbf{x}} = \Phi^\dagger \mathbf{r}$ , where  $\Phi^\dagger$  is the pseudo-inverse of the matrix  $\Phi$ . Alternative ways for solving this LS problem are to use conjugate gradient methods [29], which are known to exhibit even lower computational complexity than the pseudo inverse-based approach. We conclude by noting that the proposed relaxation entails a performance loss compared to that of (2), which cannot be solved in reasonable time. Furthermore, our simulation results in Section IV-D demonstrate the efficacy of our approach, even for complex scenes that contain occlusion.

### D. Simulation Results

In order to demonstrate the efficacy of the proposed imaging method, we next show simulation results that rely upon accurate physical models. Key in our simulation results is to generate synthetic time-domain receiver signals for scenes that contain occluded objects, i.e., the linearized model in (1) is only used for recovery but not to generate synthetic receive signals. We next detail the signal generation procedure and then show corresponding imaging results.

1) *Generation of synthetic receive signals:* Complex scenes that contain occluded objects cannot be modeled using the linearized model (1). In contrary, in practice it is of paramount importance to identify whether an object is contributing to the receive signal or not. To this end, we generate synthetic receive signals using ray-tracing, where we trace all paths from every transmitter to every receiver for a given scene and check whether the reflection is occluded or not. If a present object occludes one of the rays, the receiver would not measure the associated signal. For every path that is not occluded, we can measure the delay and attenuation (which are both functions of the propagation distance) and compute the received time-domain signal. The final received time-domain signal corresponds to a superposition of all paths that are not occluded. Note that we ignore reflections from objects to objects as the scenes considered next are fairly simple and the attenuation of such higher-order reflections is generally low. Fig. 21 illustrates the proposed ray-tracing approach. Objects in black color fully contribute to the reflected signal, while the ones shown in red

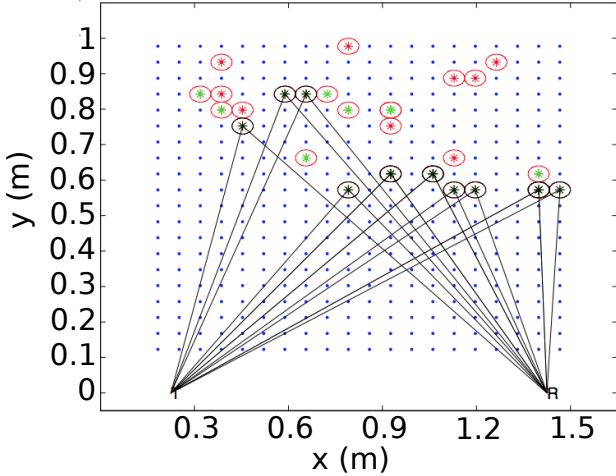


Fig. 21. Illustration of the ray-tracing method we used to synthesize the received signals in the presence of scenes with occlusions.

are occluded and do not contribute to the received signals; the green objects are partially occluded, i.e., reflections are only seen at a subset of the  $M_R$  receivers.

2) *Simulation parameters*: In order to validate the proposed linearization-based imaging approach, we consider three distinct synthetic scenes with varying complexity shown in Figure 22. Each scene models a 2-dimensional imaging area of dimension  $300 \times 500 \text{ mm}^2$ , where we discretize the area into  $40 \times 40$  cells. The simulated system is equipped with  $M_T = 10$  transmitters and  $M_R = 40$  receivers arranged on a regular linear grid; transmitters and receivers are interleaved in groups of one and four antennas, respectively. The placement of the transmit and receive antennas is shown in Fig. 22(b). We assume that all transmitters emit a Gaussian pulse (center frequency of 1.2 GHz and 50% bandwidth) at the same time instant and with the same power.

3) *Results and discussion*: Figures 22(a), (b), and (c) show the synthetic scenes. The first scene shown in (a) is occlusion free; the second scene shown in (b) contains only partial occlusion; the third scene shown in (c) contains fully occluded objects. Figures 22(d), (e), and (f) show the recovered scenes using the proposed linearization-based imaging method described in Section IV-C. Recovery of each scene only took 50 ms on an Intel i5 1.7 GHz laptop running MATLAB.

The first recovered scene in Fig. 22(d) shows that for a scene without occlusion, we can extract accurate scene information; in fact, our own results for the same scene without additive noise shows perfect recovery of this scene. The reason for this behavior is due to the fact that linearization is exact for scenes without occlusion. The second recovered scene in Fig. 22(e) shows that for a scene with partial occlusion, we are still able to faithfully recover scene of interest. We note, however, that for partially occluded objects, the result is more affected by recovery artifacts; this is mostly due to the fact that linearization is only approximating the real-world behavior and ignoring occlusion leads to interference artifacts. The third recovered scene in Fig. 22(f) shows that for a scene with fully occluded objects, our approach only

recovers scene information from objects that are either not or only partially occluded. As expected, the third layer completely disappears as its presence or absence has absolutely no effect on the received signals. These preliminary simulation results demonstrate that our linearization-based imaging approach already delivers acceptable quality, even for complex scenes with partially occluded objects at low SNR and with a simple recovery algorithm.

### E. Possible Improvements

There exist a number of techniques that will further improve the quality of our approach. For example, our own simulations have shown that by increasing the transmitters and/or receivers results renders the system less susceptible to noise and artifacts caused by partially occluded objects. Other transmit and receive array arrangements (e.g., using non-uniform antenna placement) as well as different delays and magnitudes in the transmit pulses may further enhance the quality of our results—all these methods aim at improving the conditioning of the matrix  $\Phi$ . As shown in [27], one can also include sparsity-promoting priors on the occupancy vector  $\mathbf{x}$ , e.g., by solving the so-called lasso problem [30]

$$\tilde{\mathbf{x}} = \arg \min_{\mathbf{x} \in \mathbb{R}^N} \|\mathbf{r} - \Phi \mathbf{x}\|_2^2 + \lambda \|\mathbf{x}\|_1$$

with a suitably-chosen regularization parameter  $\lambda > 0$ . We expect such sparsity-based recovery methods to further suppress noise and occlusion artifacts compared to the least-squares method used in Fig. 22. A detailed investigation of such methods, however, is left for future work.

We also note that by taking more measurements of the same scene one can reduce the effects caused by random noise but not those caused by occlusion and the linearization approach. In addition, our current approach ignores—for the sake of simplicity—different reflection properties of different objects. The development of models and algorithms that are able to handle different materials is part of ongoing research.

## V. CONCLUSION

In this paper, the technique of ultra-wideband joint spatial coding is experimentally demonstrated by generation and detection of ultra-short pulses in the frequency range 3–10 GHz. It is shown that multiple synchronized antennas, each with a broad radiation pattern, can utilize joint spatial coding to form a narrow information beam-width of  $1^\circ$ . This technique enables a secure communication link by preventing eavesdroppers from decoding the information content. It can also be used to localize point objects in 3D space with high spatial precision and to generate high-resolution 3D images of distributed objects. Furthermore, a novel mathematical approach is introduced that is capable of recovering scenes of complex distributed objects.

## ACKNOWLEDGMENTS

C. Studer would like to thank R. G. Baraniuk and G. Pope for discussions on the imaging recovery method. H. Aggrawal would like to acknowledge the help of M. Assefzadeh in the design of the impulse antennas.

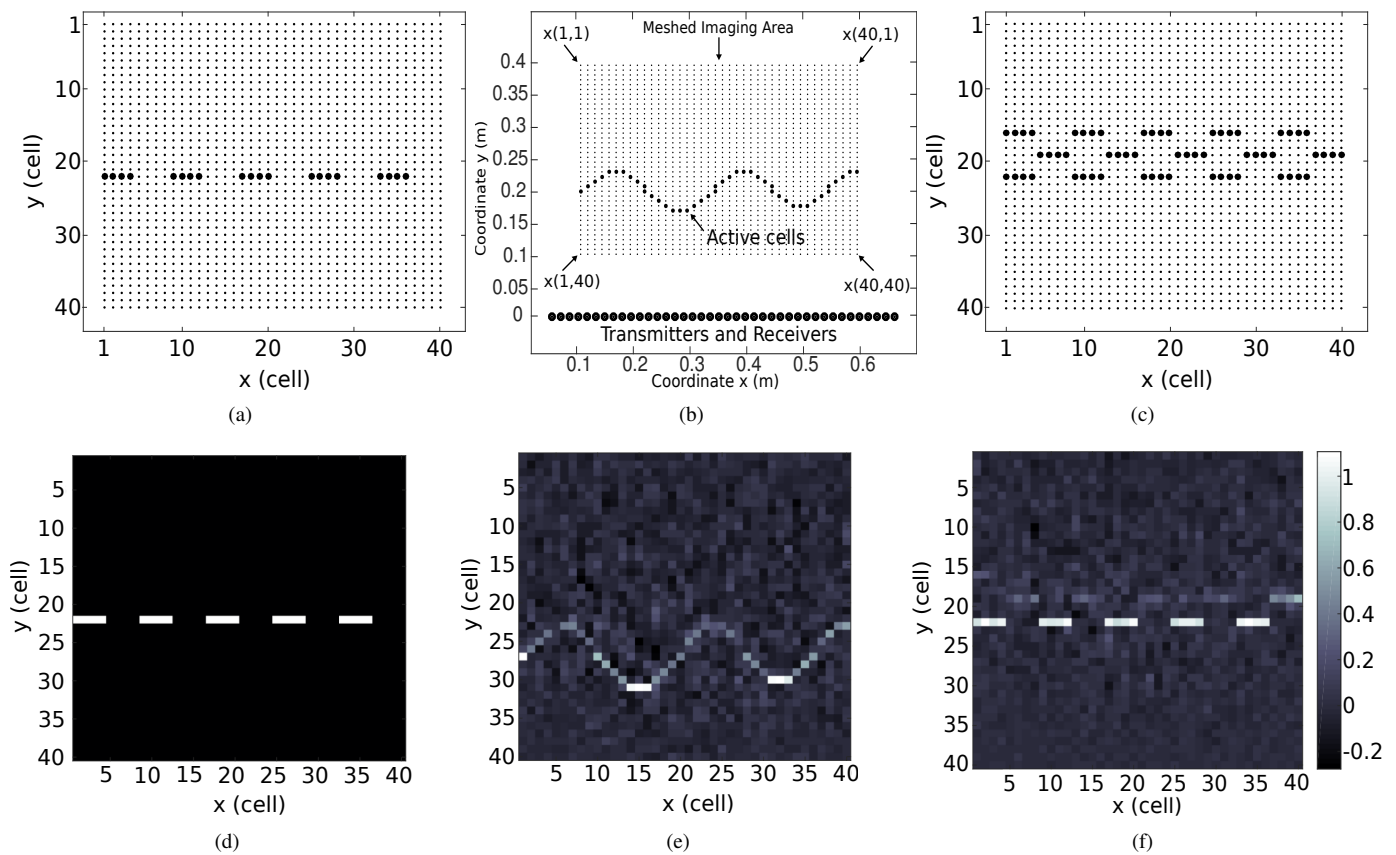


Fig. 22. Simulated and recovered scenes for a system of dimension  $300 \times 500 \text{ mm}^2$  with a  $40 \times 40$  grid. (a) scene without occlusion; (d) linearized recovery delivers excellent quality; (b) scene with partial occlusion; (e) linearized recovery is able to faithfully extract an accurate estimate; (c) scene that contains fully occluded objects; (d) linearized recovery is able to partially identify the second partially-occluded layer, whereas the fully occluded layer cannot be recovered.

## REFERENCES

- [1] H. Aggrawal, P. Chen, M. M. Assefzadeh, B. Jamali, and A. Babakhani, "Gone in a picosecond: Techniques for the generation and detection of picosecond pulses and their applications," *IEEE Microwave Magazine*, vol. 17, no. 12, pp. 24–38, Dec 2016.
- [2] H. Aggrawal, R. Puhl, and A. Babakhani, "Ultra-wideband pulse-based directional modulation," in *IEEE MTT-S International Microwave and RF Conference (IMaRC)*. Institute of Electrical and Electronics Engineers (IEEE), Dec. 2015, pp. 292–295.
- [3] P. Chen and A. Babakhani, "A 30GHz impulse radiator with on-chip antennas for high-resolution 3D imaging," in *IEEE Radio and Wireless Symposium (RWS)*, Jan. 2015, pp. 32–34.
- [4] M. M. Assefzadeh, B. Jamali, A. K. Gluszek, A. J. Hudzikowski, J. Wojtas, F. Tittel, and A. Babakhani, "Terahertz trace gas spectroscopy based on a fully-electronic frequency-comb radiating array in silicon," in *Conference on Lasers and Electro-Optics*. Optical Society of America, 2016, p. SM2L.7.
- [5] H. Aggrawal and A. Babakhani, "An ultra-wideband impulse receiver for sub-100fsec time-transfer and sub-30  $\mu\text{m}$  localization," in *2016 IEEE Radio and Wireless Symposium (RWS)*, Jan. 2016, pp. 42–44.
- [6] G. S. Shiroma, R. Y. Miyamoto, J. D. Roque, J. M. Cardenas, and W. A. Shiroma, "A high-directivity combined self-beam/null-steering array for secure point-to-point communications," *IEEE Transactions on Microwave Theory and Techniques*, vol. 55, no. 5, pp. 838–844, May 2007.
- [7] H. Aggrawal and A. Babakhani, "A 40GS/s track-and-hold amplifier with 62dB SFDR3 in 45nm CMOS SOI," in *2014 IEEE MTT-S International Microwave Symposium (IMS2014)*, Jun. 2014, pp. 1–3.
- [8] A. Babakhani, D. B. Rutledge, and A. Hajimiri, "Near-field direct antenna modulation," *IEEE Microwave Magazine*, vol. 10, no. 1, pp. 36–46, Feb. 2009.
- [9] M. P. Daly, E. L. Daly, and J. T. Bernhard, "Demonstration of directional modulation using a phased array," *IEEE Transactions on Antennas and Propagation*, vol. 58, no. 5, pp. 1545–1550, May 2010.
- [10] A. Babakhani, D. B. Rutledge, and A. Hajimiri, "Transmitter architectures based on near-field direct antenna modulation," *IEEE Journal of Solid-State Circuits*, vol. 43, no. 12, pp. 2674–2692, Dec. 2008.
- [11] I. Urazghildiev, R. Ragnarsson, and A. Rydberg, "High-resolution estimation of ranges using multiple-frequency CW radar," *IEEE Transactions on Intelligent Transportation Systems*, vol. 8, no. 2, pp. 332–339, Jun. 2007.
- [12] H. Rabe, E. Denicke, G. Armbrecht, T. Musch, and I. Rolfes, "Considerations on radar localization in multi-target environments," *Advances in Radio Science*, vol. 7, pp. 5–10, 2009.
- [13] R. Berenguer, G. Liu, A. Akhijat, K. Kamtikar, and Y. Xu, "A 43.5mW 77GHz receiver front-end in 65nm CMOS suitable for FM-CW automotive radar," in *IEEE Custom Integrated Circuits Conference 2010*, Sep. 2010, pp. 1–4.
- [14] N. Obeid, M. Heddebaut, F. Boukour, C. Loyez, and N. Rolland, "Millimeter wave ultra wide band short range radar localization accuracy," in *VTC Spring 2009 - IEEE 69th Vehicular Technology Conference*, Apr. 2009, pp. 1–5.
- [15] M. Malanowski and K. Kulpa, "Two methods for target localization in multistatic passive radar," *IEEE Transactions on Aerospace and Electronic Systems*, vol. 48, no. 1, pp. 572–580, Jan. 2012.
- [16] A. M. Zelnio and B. D. Rigling, "Detection-based localization of passive radar receivers," in *IEEE Radar Conference*, May 2012, pp. 0173–0177.
- [17] Y. Ju, Y. Jin, and J. Lee, "Design and implementation of a 24 GHz FMCW radar system for automotive applications," in *2014 International Radar Conference*, Oct. 2014, pp. 1–4.
- [18] T. Mitomo, N. Ono, H. Hoshino, Y. Yoshihara, O. Watanabe, and I. Seto, "A 77 GHz 90 nm CMOS transceiver for FMCW radar applications," *IEEE Journal of Solid-State Circuits*, vol. 45, no. 4, pp. 928–937, Apr. 2010.
- [19] G. Wei, Y. Zhou, and S. Wu, "Detection and localization of high speed moving targets using a short-range UWB impulse radar," in *2008 IEEE Radar Conference*, May 2008, pp. 1–4.
- [20] A. O. Boryszenko, C. Craeye, and D. H. Schaubert, "Ultra-wide band

- near-field imaging system,” in *2007 IEEE Radar Conference*, Apr. 2007, pp. 402–407.
- [21] Y. Yang and A. Fathy, “Design and implementation of a low-cost real-time ultra-wide band see-through-wall imaging radar system,” in *2007 IEEE/MTT-S International Microwave Symposium*, Jun. 2007, pp. 1467–1470.
- [22] F. Adib and D. Katabi, “See through walls with WiFi!” in *Proceedings of the ACM SIGCOMM 2013 Conference on SIGCOMM*. New York, NY, USA: ACM, 2013, pp. 75–86.
- [23] S. S. Ram and H. Ling, “Through-wall tracking of human movers using joint Doppler and array processing,” *IEEE Geoscience and Remote Sensing Letters*, vol. 5, no. 3, pp. 537–541, Jul. 2008.
- [24] T. S. Ralston, G. L. Charvat, and J. E. Peabody, “Real-time through-wall imaging using an ultrawideband multiple-input multiple-output (MIMO) phased array radar system,” in *2010 IEEE International Symposium on Phased Array Systems and Technology*, Oct. 2010, pp. 551–558.
- [25] S. S. Fayazi, J. Yang, and H. S. Lui, “UWB SAR imaging of near-field object for industrial process applications,” in *2013 7th European Conference on Antennas and Propagation (EuCAP)*, Apr. 2013, pp. 2245–2248.
- [26] H. K. Bidhendi, H. M. Jafari, and R. Genov, “Ultra-wideband imaging systems for breast cancer detection,” in *Ultra-Wideband and 60 GHz Communications for Biomedical Applications*. Springer, Jan. 2014.
- [27] G. Pope, M. Lerjen, S. Mullener, S. Schlapfer, T. Walti, J. Widmer, and C. Studer, “Light curtain localization via compressive sensing,” in *2013 IEEE International Conference on Acoustics, Speech and Signal Processing*, May 2013, pp. 2558–2562.
- [28] E. Agrell, T. Eriksson, A. Vardy, and K. Zeger, “Closest point search in lattices,” *IEEE Transactions on Information Theory*, vol. 48, no. 8, pp. 2201–2214, Aug. 2002.
- [29] J. R. Shewchuk, “An introduction to the conjugate gradient method without the agonizing pain,” Pittsburgh, PA, USA, Tech. Rep., 1994.
- [30] R. Tibshirani, “Regression shrinkage and selection via the lasso: a retrospective,” *Journal of the Royal Statistical Society: Series B (Statistical Methodology)*, vol. 73, no. 3, pp. 273–282, 2011.